PAPER

Check for updates

Macrophage membrane coated persistent luminescence nanoparticle@MOF-derived mesoporous carbon core–shell nanocomposites for autofluorescence-free imaging-guided chemotherapy†

Li-Jian Chen, [ID] [ab] Xu Zhao, [ID] [ab] Yao-Yao Liu[b] and Xiu-Ping Yan [ID] *[abcd]

Efficient drug nanocarriers with high drug loading capacity and luminescent ability are in high demand for biomedical applications. Here we show a facile and bio-friendly synthesis of macrophage membrane coated persistent luminescence nanoparticle (PLNP)@metal–organic framework (MOF)-derived mesoporous carbon (MC) core–shell nanocomposites (PLMCs) for autofluorescence-free imaging-guided chemotherapy. MOF UiO-66 is used as both the precursor and the template, and is controllably coated on the surface of the PLNP to form a PLNP@UiO-66 core–shell composite. Subsequent calcination enables the transformation of PLNP@UiO-66 to PLMC due to the pyrolysis of the UiO-66 shell. PLMC with a small particle size of 70 nm, a tunable large pore size from ∼4.8 to ∼16.2 nm in the shell and near-infrared persistent luminescence in the core was prepared by controlling the calcination conditions. The prepared PLMC showed an enhanced drug loading capacity for three model drugs (doxycycline hydrochloride, acetylsalicylic acid, and paclitaxel) compared with PLNP@UiO-66. Further coating of the macrophage membrane on the surface of PLMC results in MPLMC with enhanced cloaking ability for evading the mononuclear phagocyte system. The drug-loaded MPLMC is promising for autofluorescence-free persistent luminescence imaging-guided drug delivery and tumor therapy.

Introduction

Nanoparticle-based drug delivery systems have emerged as powerful carriers for breaking pharmacokinetic limitations such as short drug half-lives and systemic side effects brought by traditional free drugs.[1] However, drug carrier transport in a complicated biological environment is hard to monitor in real-time, while their ineffective aggregates in diseased sites lead to poor therapeutic efficacy and undesirable adverse effects.[2] Endowing drug carriers with luminescent properties is an effective and simple way to visualize the transport routes in real-time. Fluorescent reagents such as organic dyes,[3] quantum dots (QDs),[4] and upconversion luminescent nanoparticles (UCNPs) have been used to label drug carriers in living systems.[5] However, organic dyes suffer from an inherent photobleaching problem. The need for constant *in situ* excitation for conventional QDs is liable to cause autofluorescence interference and tissue damage. UCNPs can effectively avoid autofluorescence, but still need constant *in situ* excitation.

Persistent luminescence nanoparticles (PLNPs) have attracted considerable attention as biomedical imaging materials.[6–10] PLNPs are capable of energy storage under various light excitation (X-ray, sunlight, UV-visible light, and red light emitting diode (LED) light) conditions to emit long lifetime luminescence after the excitation stops, thereby allowing time-resolved imaging to eliminate tissue autofluorescence.[11–14] Recently, nanocomposites of near-infrared (NIR) PLNPs with micro/mesoporous structures such as mesoporous SiO₂ nanoparticles have been explored for autofluorescence-free persistent luminescence imaging-guided drug delivery and tumor therapy.[15–19] However, mesoporous silica nanoparticles are biocompatible and hydrophilic but show poor affinity to hydrophobic drugs, limiting their applications as nanocarriers to load hydrophobic drugs.[20]

a State Key Laboratory of Food Science and Technology, Jiangnan University, Wuxi 214122, China. E-mail: xpyan@jiangnan.edu.cn

b Institute of Analytical Food Safety, School of Food Science and Technology, Jiangnan University, Wuxi 214122, China

c International Joint Laboratory on Food Safety, Jiangnan University, Wuxi 214122, China

d Key Laboratory of Synthetic and Biological Colloids, Ministry of Education, Jiangnan University, Wuxi 214122, China

† Electronic supplementary information (ESI) available. See DOI: 10.1039/d0tb01272f

Metal–organic frameworks (MOFs), built with metal ions or clusters and organic linkers as bridges, have attracted great attention in drug delivery vessel applications owing to their high specific surface area, low cost, and well-designed functionalities.[21,22] A chromium-doped zinc gallogermanate PLNP was combined with a zeolitic imidazolate framework-8 (ZIF-8) to construct a core–shell multifunctional nanoplatform as an NIR persistent luminescence trackable drug delivery vehicle for the anti-cancer drug doxorubicin (Doxo).[23,24] However, Doxo with a kinetic diameter of ca. $1.5 \times 1.0 \times 0.7$ nm was merely adsorbed (or anchored) on the external surface of the ZIF-8 with a small pore window (ca. 0.34 nm).[25] The difficulty in loading large-sized drugs due to the insufficient pore size and accessibility of MOF cavities limits the application of ZIF-8 as drug carriers. An MIL-100 MOF with a sufficient pore size of about 2.9×2.5 nm could load cidofovir, azidothymidine triphosphate, busulfan, and Doxo.[26] MIL-101-NH$_2$ with a larger pore size ($\sim 3.4 \times 2.9$ nm) showed enhanced loading capacity for azidothymidine triphosphate and cidofovir.[26] Even so, MOF-based drug carriers still have a few shortcomings, such as cytotoxicity, instability under physiological conditions, and poor colloidal stability.[27]

Mesoporous carbon (MC) nanospheres/nanoparticles are emerging materials for drug delivery due to advantages such as non-toxic nature, tunable pore size, high monodispersity, and controllable morphology and surface properties.[28,29] MC with a uniform particle size of 150 nm (pore size: ~ 2.1 nm) prepared using a MCM-48 type mesoporous silica template method was used as a drug carrier for camptothecin ($1.3 \times 0.8 \times 0.7$ nm).[30] A hollow-structured MC nanocapsule with a hydrodynamic size of 306 nm prepared using an extended Stöber method with colloidal silica as the template was applied for Doxo delivery.[31] A core–shell MC@silica composite (200 nm) with dual-ordered mesopores of 3.1 and 5.8 nm was prepared by an in situ coating and selective etching method for the delivery of hydrophilic cisplatin and hydrophobic paclitaxel (PTX) in multidrug therapy.[20] The removal of silica templates using hazardous reagents such as alkali solution and HF is the main drawback of template methods for the preparation of MC, which limits their extensive use.[32,33] Furthermore, downsizing MC less than 100 nm is still appealing owing to the optimal size of the transmembrane delivery vehicle which should be smaller than 100 nm in diameter.[34] MOF-derived porous carbon nanoparticles show great potential in gas adsorption, water treatment, and electrochemical energy storage as well as catalyst supports because of the advantages of controllable shape and size and well-designed functionalities.[35–37] However, to the best of our knowledge, MOF-derived MCs for drug delivery have not been reported to date.

Herein, we report macrophage membrane coated persistent luminescence nanoparticle (PLNP)@metal–organic framework (MOF)-derived mesoporous carbon (MC) core–shell nanocomposites (PLMCs) for autofluorescence-free imaging-guided chemotherapy. A facile surface MOF coating with the subsequent calcination strategy is developed for the preparation of PLMC. As a proof of concept, we take UiO-66 as a model MOF to serve as the precursor and the template due to its relatively large pore size, good stablility and easy synthesis. The developed synthesis strategy produces PLMC with a small particle size of ~ 70 nm, a tunable mesopore size from ~ 4.8 to ~ 16.2 nm and long NIR persistent luminescence without the need for hazardous reagents to remove the template. Furthermore, the biomimetic macrophage membrane camouflage of PLMC (MPLMC) increases the circulation time and the targeting ability. The as-prepared MPLMC shows great potential as persistent luminescence trackable nanocarriers for the efficient delivery of drugs, biomacromolecules or other guest molecules, especially large-sized guests.

Experimental

Synthesis of the oleate-capped PLNP

The $Zn_{1.1}Ga_{1.8}Ge_{0.1}O_4$:0.5% Cr^{3+} PLNP was synthesized according to the modified solvothermal method.[38,39] Typically, NaOH (0.3 g), H$_2$O (4 mL), ethanol (9 mL), and oleic acid (3 mL) were gently mixed, and then solutions of $Zn(NO_3)_2$ (550 μL, 0.5 mol L^{-1}), $Ga(NO_3)_3$ (900 μL, 0.5 mol L^{-1}), $Cr(NO_3)_3$ (45 μL, 0.05 mol L^{-1}) and $Ge(IV)$ solution (63 μL, 0.4 mol L^{-1}) were added dropwise and vigorously stirred after adjusting the pH to 8.0 with ammonia hydroxide for another 1 h. $Ge(IV)$ solution was pre-prepared according to a previous publication.[40] The mixture was transferred to a Teflon-lined autoclave and heated to 220 °C for 16 h. The product was washed with ethanol and cyclohexane separately three times, and collected via centrifugation. Then oleate-capped PLNP was obtained.

Carboxylic acid group anchoring to the PLNP

To synthesize PLNP@UiO-66, the carboxylic acid group was first anchored to the PLNP replacing the oleic ligands. Typically, the above prepared oleate-capped PLNP was dispersed in 4 mL of tetrahydrofuran and added into 8 mL of tetrahydrofuran containing 50 mg of 3,4-dihydroxyhydrocinamic acid. The mixed solution was heated to 50 °C, stirred for 3 h, and cooled down to the temperature naturally. The carboxylic acid-capped PLNP (PLNP-COOH) was washed with ethanol three times and dispersed in DMF for further use.

Synthesis of UiO-66 nanoparticles

ZrCl$_4$ (21 mg) in a mixed solvent of DMF : ethanol (14 mL : 3 mL) was mixed with PTA (15 mg) in a mixed solvent of DMF : ethanol (13 mL : 6 mL). The mixed solution was heated in an oil bath at 100 °C for 5 h. The product was finally washed with ethanol several times, and UiO-66 nanoparticles were obtained.

A typical synthesis of PLNP@UiO-66

In a typical synthesis of PLNP@UiO-66, 21 mg of ZrCl$_4$ in a mixed solvent of DMF : ethanol (14 mL : 3 mL) was introduced dropwise into 6 mL of DMF containing the above prepared PLNP-COOH under sonication. Then, 15 mg of p-phthalic acid (PTA) in a mixed solvent of DMF : ethanol mixture (7 mL : 6 mL) was added dropwise to the mixture. The resulting solution was heated in an oil bath at 100 °C for 5 h.

Effect of solvent composition on the synthesis of PLNP@UiO-66

Four copies of $ZrCl_4$ (21 mg) in different compositions of solvents: DMF (23 mL), mixed DMF and ethanol (14 mL : 3 mL), mixed DMF and ethanol (14 mL : 6 mL), and mixed DMF and ethanol (11 mL : 9 mL) were, respectively, introduced dropwise into 6 mL of DMF containing the above prepared carboxylic acid-capped PLNP under sonication. Then, four copies of PTA (15 mg) in different compositions of solvents: DMF (10 mL), mixed DMF and ethanol (7 mL : 6 mL), mixed DMF and ethanol (7 mL : 6 mL), and mixed DMF and ethanol (7 mL : 6 mL) were, respectively, added to the mixture dropwise. The resulting solution was heated in an oil bath at 100 °C for 5 h.

Effect of reaction temperature on the synthesis of PLNP@UiO-66

Two copies of $ZrCl_4$ (21 mg) in a mixed solvent of DMF and ethanol (14 mL : 3 mL) were respectively introduced dropwise into 6 mL of DMF containing the above prepared carboxylic acid-capped PLNP under sonication. Then, two copies of PTA (15 mg) in a mixed solvent of DMF and ethanol (7 mL : 6 mL) were respectively added dropwise to the mixture. The resulting solution was heated to different temperatures (120 °C and 140 °C, respectively) in an oil bath for 5 h.

Effect of the weight ratio of the reactants on the synthesis of PLNP@UiO-66

Two pieces with different weights of $ZrCl_4$ (10.5 mg; 42 mg) in a mixed solvent of DMF and ethanol (14 mL : 3 mL) were respectively introduced dropwise into 6 mL of DMF containing the above prepared carboxylic acid-capped PLNP under sonication. Then, two pieces with different weights of PTA (7.5 mg; 30 mg) in a mixed solvent of DMF and ethanol (7 mL : 6 mL) were respectively added to the mixture dropwise. The resulting solution was heated in an oil bath at 100 °C for 5 h.

Effect of reaction time on the synthesis of PLNP@UiO-66

Two copies of $ZrCl_4$ (21 mg) in a mixed solvent of DMF and ethanol (14 mL : 3 mL) were introduced dropwise into 6 mL of DMF containing the above prepared carboxylic acid-capped PLNP under sonication. Then, three copies of PTA (15 mg) in a mixed solvent of DMF and ethanol (7 mL : 6 mL) were respectively added to the mixture dropwise. The resulting solution was transferred to a Teflon-lined autoclave and heated to 100 °C at different times (2 h, 5 h, and 8 h, respectively).

Effect of different calcination conditions on the formation of PLMC

The typical PLNP@UiO-66 with a shell thickness of 18 nm prepared with $ZrCl_4$ (21 mg) and PTA (15 mg) in a mixed solvent of DMF and ethanol (27 mL : 9 mL) after the reaction at 100 °C for 5 h were calcinated in an air atmosphere under different conditions: 400 °C for 1 h, 500 °C for 1 h, 500 °C for 2 h, 500 °C for 3 h, 600 °C for 1 h, and 800 °C for 1 h, respectively. The TEM images, photoluminescence spectra, specific surface area, and pore width distribution of those products were respectively studied.

Cell culture and imaging

SCC-7 squamous epithelial cancer cells and J774A.1 macrophages were cultured in DMEM medium with 10% FBS and 1% penicillin–streptomycin (PS). Human umbilical vascular endothelial cells (HUVECs) were cultured in Ham's F-12K medium with 100 μg mL^{-1} heparin, 50 μg mL^{-1} ECGs, 10% FBS and 1% PS. All the cells were cultured in 5% CO_2 at 37 °C. The SCC-7 cells were adhered to a confocal dish overnight and incubated with DiO processed MPLMC or PLMC for 12 h. The cells were washed with PBS and fixed in 4% paraformaldehyde, and stained with DAPI before cell imaging. The J774A.1 macrophages were adhered to a confocal dish overnight and incubated with MPLMC or PLMC for 12 h. The cells were washed with PBS and fixed in 4% paraformaldehyde, and stained with DAPI before cell imaging.

Transwell assay

The SCC-7 cells were seeded at 1×10^5 cells per well in 24-well plates. HUVECs were seeded at 1.5×10^4 cells per filter on transwell inserts (pore size, 8 μm) in a blank well and activated with or without tumor necrosis factor-α (TNF-α) (10 ng mL^{-1}) for 4 h. Then, the transwell inserts with HUVECs were introduced with MPLMC or PLMC and transferred into the wells seeded with SCC-7, and the two cells were co-cultured for another 12 h. Finally, the SCC-7 cells in the lower chamber were fixed with 4% paraformaldehyde and stained with DAPI before imaging.

In vivo imaging of SCC-7 tumor-bearing mice

All animal experiments followed the rules of Jiangnan University of Use and Care of Laboratory Animals. The animal ethical committee of the Jiangnan University approved the experiments and gave an accreditation number of JN.No20180615b0 181030[106]. Athymic nude mice (Balb/c, female, 5 weeks old) were subcutaneously injected with SCC-7 (5×10^6 cells) to produce tumors. MPLMC or PLMC (200 μL, 2.5 mg mL^{-1} as PLMC) dispersion in PBS (10 mmol L^{-1}, pH 7.4) was intravenously injected into anesthetized tumor-bearing mice. Before acquiring persistent luminescence images at different times the mice were subject to two minutes of LED light (650 ± 10 nm, 5000 lumens) illumination. The images were captured in the luminescence imaging mode, while the excitation filter was blocked and the emission filter was open.

In vivo therapeutic effect

Balb/c nude mice bearing SCC-7 tumors (tumor size ∼3–5 mm) were randomly divided into four groups ($n = 5$). MPLMC-PTX (200 μL, 2.5 mg mL^{-1} as PLMC) was intravenously injected into the mice in the experiment group once every two days for two times. The other three groups injected with PLMC-PTX, MPLMC and PBS were used as the control. The tumor length and width were measured using a vernier caliper every two days for 14 days. The tumor volumes were calculated based on the length × width^2/2.

Results and discussion

Design of drug-loaded MPLMC for autofluorescence-free imaging-guided chemotherapy

Scheme 1a illustrates the design and preparation of the drug-loaded MPLMC. To achieve autofluorescence-free *in vivo* imaging, the $Zn_{1.1}Ga_{1.8}Ge_{0.1}O_4$:$Cr^{3+}$ PLNP was used as the persistent luminescent source due to its ultralong NIR persistent luminescence and LED light-renewable ability.[40] The PLNP@UiO-66 core–shell nanocomposite was then designed *via* an *in situ* surface coating strategy. For this purpose, the carboxylic acid group was anchored on the surface of the oleate-capped PLNP to form PLNP-COOH as a suitable building block for subsequent growth of the UiO-66 shell. The formation of the UiO-66 shell on the surface of PLNP-COOH was initiated by heterogeneous nucleation and driven by chelation between Zr^{4+} ions and the organic linker *p*-phthalic acid (PTA) with the aid of the carboxylic coordination group. As such, the NIR persistent luminescence of PLNP was almost quenched by the UiO-66 shell due to its strong and wide absorption.

To improve the bioimaging ability and the drug loading capacity, the PLNP@UiO-66 core–shell nanocomposite was calcinated at a high temperature to obtain PLMC. Thus, UiO-66 was turned into mesoporous carbon containing Zr metal centers in the shell for loading drugs, while the NIR persistent luminescence from PLNP in the core was recovered for the resultant PLMC due to the transformation of UiO-66 to MC. To further increase the circulation time and the targeting ability, the J774A.1 macrophage membrane was coated on the drug-loaded PLMC after sonication and electrostatic adhesion to produce drug-loaded MPLMC. The drug-loaded MPLMC was thus designed for *in vivo* autofluorescence-free imaging-guided tumor therapy (Scheme 1b).

Synthesis and characterization of the PLNP and PLNP@UiO-66

The $Zn_{1.1}Ga_{1.8}Ge_{0.1}O_4$:$Cr^{3+}$ PLNP was prepared *via* a solvothermal method.[38,39] The prepared PLNP was uniform with an average size of 34.4 ± 7.1 nm (based on the 100 randomly selected nanoparticles) (Fig. 1c) and a fine cubic spinel structure of Zn_2GeO_4 (JCPDS 25-1018) and $ZnGa_2O_4$ (JCPDS 38-1240) (Fig. 1a). The as-prepared PLNP exhibited NIR luminescence emission at 700 nm ($^2E \rightarrow {}^4A_2$ transition) and excitation bands at 240 nm (band-to-band transition), 420 nm ($^2A_2 \rightarrow {}^4T_1$ transition), and 550 nm ($^2A_2 \rightarrow {}^4T_2$ transition) (Fig. 1b). In addition, the PLNP exhibited good persistent luminescence after 10 min of UV light excitation and ultralong persistent luminescence (Fig. S1 and S2, ESI†). The persistent luminescence of PLNP can be repeatedly activated using a red LED lamp (650 ± 10 nm), and is still detectable at 48 h after 2 min of LED illumination (Fig. S3 and S4, ESI†).

To prepare the PLNP@UiO-66 core–shell structures, the carboxylic acid group was first anchored on the surface of the PLNP with 3,4-dihydrohydrocinamic acid as the guest ligand. As a result, the Zr ions in the UiO-66 shell chelated with the carboxylic acid group on the surface of the PLNP first. Small UiO-66 clusters formed small crystals or sol particles, and then dissolved and re-deposited on the surface of the larger particles *via* the Ostwald ripening process,[41] and finally produced the PLNP@UiO-66 core–shell structures.

The effect of DMF or its combination with ethanol as the solvent was investigated on the formation of the uniform core–shell nanostructures *via* TEM monitoring (Fig. 1b–e). It is noted that the PLNP@UiO-66 core–shell structures failed to form in pure DMF (Fig. 1b). However, a mixed solvent of DMF : ethanol (27 mL : 9 mL; 27 mL : 12 mL) resulted in uniform core–shell
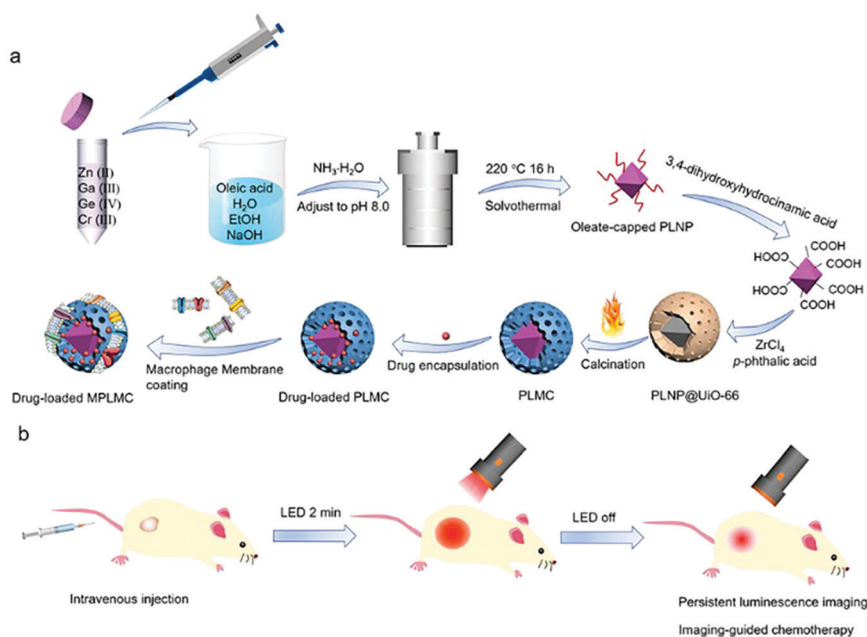
Scheme 1 Schematic illustration of the drug-loaded MPLMC for theranostics: (a) design and synthesis and (b) application for *in vivo* autofluorescence-free imaging-guided chemotherapy.
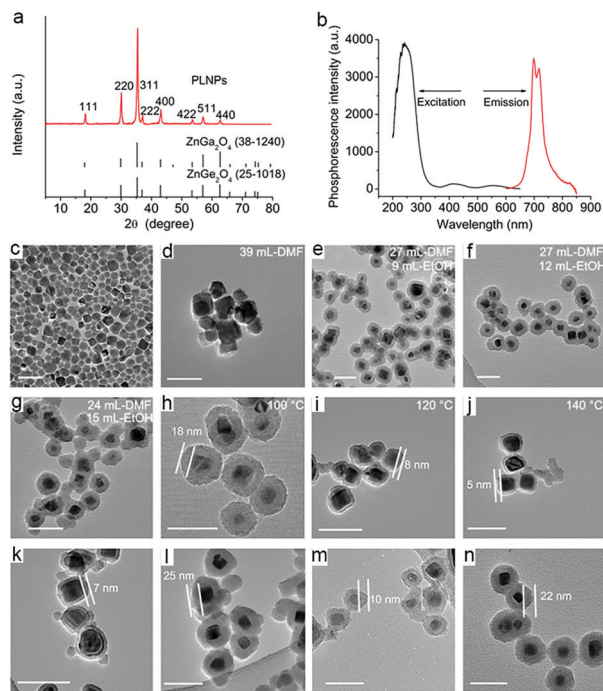
Fig. 1 (a) XRD pattern of the prepared PLNP. (b) Phosphorescence excitation and emission spectra of PLNP. TEM images: (c) the as-prepared PLNP; (d–g) PLNP@UiO-66 prepared in various solvents at 100 °C after the reaction for 5 h; (h–j) PLNP@UiO-66 prepared in a mixed solvent of DMF : ethanol (27 mL : 9 mL) at different temperatures after the reaction for 5 h; (k and l) PLNP@UiO-66 prepared with half and double weight compositions of $ZrCl_4$: terephthalic acid precursors (10.5 mg : 7.5 mg; 42 mg : 30 mg, respectively) in a mixed solvent of DMF : ethanol (27 mL : 9 mL) at 100 °C after the reaction for 5 h. (m and n) PLNP@UiO-66 prepared in a mixed solvent of DMF : ethanol (27 mL : 9 mL) at 100 °C after the reaction for 2 and 8 h, respectively. Scale bar: 100 nm.

nanostructures (Fig. 1c and d), while a mixed solvent of DMF : ethanol (24 mL : 15 mL) produced disordered core–shell nanostructures (Fig. 1e). The results indicate that a small amount of ethanol significantly facilitated the formation of the PLNP@UiO-66 core–shell structures.

The effect of the reaction temperature on the growth of the UiO-66 shell on the surface of the PLNP was further investigated. In a typical experiment, the UiO-66 layer was prepared with $ZrCl_4$ (21 mg) and PTA (15 mg) in a mixed solvent of DMF : ethanol (27 mL : 9 mL) containing PLNP-COOH and incubated at 100 °C with reflux for 5 h. Well-dispersed uniform core–shell PLNP@UiO-66 with a layer of 18 nm was thus obtained (Fig. 1f). However, the thickness of the UiO-66 shell decreased to 8 nm and 5 nm when the reaction temperature changed to 120 °C and 140 °C, respectively (Fig. 1g and h). Thus, the mixed solutions were incubated in a 100 °C oil bath with reflux to form uniform PLNP@UiO-66 (Fig. 1f). Furthermore, the UiO-66 shell thickness can also be controlled by adjusting the amount of the UiO-66 precursors (Fig. 1i and j) and the reaction time (Fig. 1k and l).

The prepared PLNP@UiO-66 with a shell thickness of 18 nm was further characterized through elemental mapping, XRD pattern, and N_2 sorption isotherms. Elemental mapping

demonstrates the elements Zn, Ga and Ge in the core and elements C and Zr in the shell, and element O in the whole nanostructures (Fig. 2a–h), proving the core–shell structure of PLNP@UiO-66. The as-prepared PLNP@UiO-66 showed a diffraction peak at ~8° similar to the prepared UiO-66, matching the two peaks at 7.4° and 8.5° featured in the simulated PXRD pattern of UiO-66 (Fig. 2i). The characteristic of the N_2 type-IV sorption isotherms shows that the introduction of porous UiO-66 has a significant effect on the surface area and the porosity of PLNP@UiO-66 (Fig. 2j and Fig. S5, ESI†). The Brunauer–Emmett–Teller (BET) surface area increased from 8 m^2 g^{-1} (PLNP) to 371 m^2 g^{-1} (PLNP@UiO-66) (Table 1). The pore size distribution based on the Barrett–Joyner–Halenda (BJH) model reveals the major pores at 1.1 nm (octahedral) of PLNP@UiO-66 similar to those of the prepared UiO-66 nanoparticles (the inset of Fig. 2j and Fig. S6, ESI†). The total pore volume of PLNP@UiO-66 was 0.803 cm^3 g^{-1} (Table 1).

The prepared PLNP@UiO-66 exhibited almost no luminescence due to the quenching effect of the UiO-66 shell with broad-spectrum absorption on the NIR luminescence of the PLNP *via* Förster resonance energy transfer (Fig. 2k and Fig. S7, S8, ESI†). Although the persistent luminescence of PLNP@UiO-66 after 2 min of LED illumination can be detected for up to 6 h (the inset of Fig. 2k), the luminescence signal is too weak for *in vivo* imaging applications. Meanwhile, the insufficient pore size of 1.1 nm limits the application of PLNP@UiO-66 as a drug carrier for large-sized drugs.

To solve these problems, calcination treatment was adopted to transform PLNP@UiO-66 into PLMC. Thermogravimetric analysis (TGA) was used to seek guidance for the preparation of PLMC. The TGA curves of PLNP-COOH and PLNP@UiO-66 show weight loss of 5% and 28% at 800 °C, respectively (Fig. 2l).

The TGA curve of PLNP@UiO-66 exhibited high thermal stability up to 400 °C but a sharp decrease of weight at *ca.* 500 °C mainly due to the pyrolysis of the organic linker PTA in the UiO-66 frameworks. Thus, the calcination temperatures around 500 °C were selected to study the effect on the PLMC in subsequent experiments.

Preparation and characterization of PLMC

The effect of the calcination temperature was investigated in the range of 400–800 °C to transform PLNP@UiO-66 into PLMC with a suitable mesopore and strong luminescence. 1 h of calcination at 400 °C did not lead to obvious changes in the morphology (Fig. 3a), the XRD pattern (Fig. 3e), the luminescence emission (Fig. 3f), the BET surface area and the pore volume (Fig. 3g and Table 1). Besides, the major types of pores at 1.1 nm for UiO-66 remained and no mesoporous pores appeared after 1 h of calcination at 400 °C (the inset of Fig. 3g). These results indicate no obvious change of PLNP@UiO-66 after 1 h of calcination at 400 °C. Meanwhile, 1 h of calcination of PLNP@UiO-66 at 800 °C resulted in an agglomerated and lumpy morphology (Fig. 3d), a zirconia crystal phase with characteristic XRD peaks at 30.2°, 50.5°, and 60.2° for the tetragonal zirconia structure (Fig. 3e),[42] and a decreased BET surface area and pore volume, but nearly no micro/mesopores
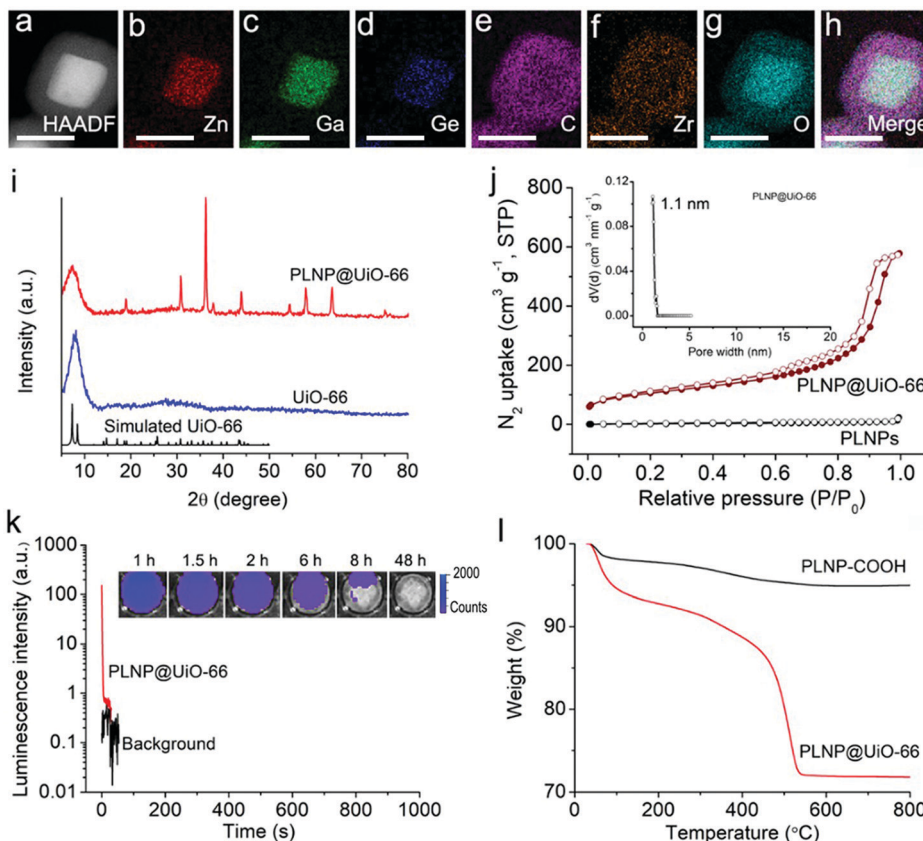
Fig. 2 Characterization of the prepared PLNP@UiO-66 with a shell thickness of 18 nm: (a) high-angle annular dark field (HAADF) imaging; (b) Zn elemental mapping, (c) Ga elemental mapping, (d) Ge elemental mapping, (e) C elemental mapping, (f) Zr elemental mapping, (g) O elemental mapping, and (h) Zn, Ga, Ge, C, Zr and O composite elemental mapping, scale bar = 50 nm; (i) XRD patterns; and (j) N$_2$ adsorption–desorption isotherms. The inset shows the pore size distribution; (k) persistent luminescence decay curves monitored at 700 nm after pre-excitation with a UV lamp for 10 min, and the inset shows afterglow images recorded on an IVIS Lumina III imaging system (100 mg in powder) and (l) TGA curves.

Table 1 BET surface area, pore volume and pore size distribution of PLNP, UiO-66, PLNP@UiO-66, and the products obtained from PLNP@UiO-66 after different calcination conditions

	BET surface area (m^2 g^{-1})	Pore volume (cm^3 g^{-1})	Pore size (nm)
PLNP	8	—	—
UiO-66	356	0.317	1.1
PLNP@UiO-66	371	0.803	1.1
1 h calcination of PLNP@UiO-66 at 400 °C	322	0.930	1.1
1 h calcination of PLNP@UiO-66 at 500 °C	133	0.478	4.8; 10.9
1 h calcination of PLNP@UiO-66 at 600 °C	118	0.546	10.7
1 h calcination of PLNP@UiO-66 at 800 °C	77	0.297	—
2 h calcination of PLNP@UiO-66 at 500 °C	131	0.468	7.6; 16.2
3 h calcination of PLNP@UiO-66 at 500 °C	126	0.437	7.6; 16.2

(Fig. 3g and Table 1), indicating that PLMC was not produced after calcination at 800 °C.

In contrast, 1 h of calcination at 500 °C or 600 °C resulted in a hydrangea-like porous morphology with a particle size of *ca.* 70 nm (Fig. 3b and c), and a reduced BET surface area and

pore volume (Fig. 3g and Table 1). Two types of mesopores centered at ∼4.8 nm and ∼10.9 nm appeared after calcination at 500 °C for 1 h, while one type of mesopore centered at ∼10.7 nm appeared after calcination at 600 °C for 1 h (the inset of Fig. 3g). The characteristic XRD pattern for the UiO-66 lattice structure disappeared, but the crystalline structure of PLNP still existed and two new broad peaks appeared at ∼52° and ∼60° after calcination at 500 °C or 600 °C (Fig. 3e), which is mainly attributed to the collapse of the UiO-66 lattice structure and the formation of the zirconia structure. Besides, calcination at 500 °C or 600 °C for 1 h resulted in strong NIR luminescence emission (Fig. 3f). Correspondingly, the UiO-66-derived MC nanoparticles obtained after calcination at 500 °C for 1 h showed lower absorbance than UiO-66 at the same concentration at 520–900 nm (Fig. S8, ESI†), resulting in luminescence recovery. The results prove the formation of mesopores and the successful transformation of PLNP@UiO-66 to PLMC under calcination at 500 or 600 °C.

To further regulate the pore size distribution, the effect of calcination time was studied at a calcination temperature of 500 °C. 2- and 3-h calcination resulted in similar morphologies (Fig. S9 and S10, ESI†), XRD patterns (Fig. S11, ESI†) and luminescence emission spectra (Fig. S12, ESI†), and almost
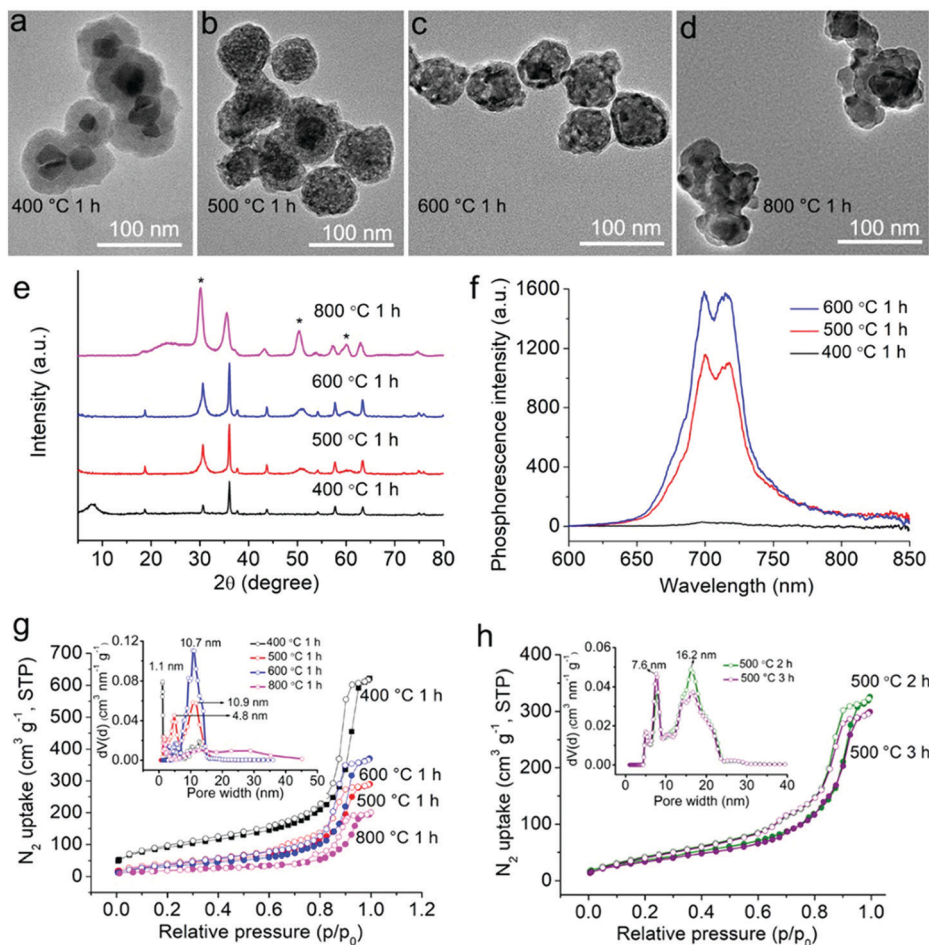
Fig. 3 Characterization of PLMC and its products obtained under different calcination conditions: (a–d) TEM images; (e) XRD patterns; (f) phosphorescence emission spectra (1 mg mL^{-1} in dispersion); and (g and h) N$_2$ adsorption–desorption isotherms and the insets show the pore size distribution.

the same BET surface areas and pore volumes (Fig. 3h and Table 1) compared with those obtained during 1 h of calcination. However, different types of mesopores centered at ~7.6 nm and ~16.2 nm were observed after 2- or 3 h of calcination (the inset of Fig. 3h). An increase of the calcination time from 1 h to 3 h resulted in an increased proportion of the mesopore size at ~7.6 nm but a decreased proportion of the mesopore size at ~16.2 nm (the inset of Fig. 3h). Thus, PLMC with different mesopore size distributions from ~4.8 nm to ~16.2 nm was obtained after calcination at 500 °C or 600 °C upon controlling the calcination time. The magnified HRTEM images and particle dispersion were also compared to display the difference in the morphology and the hydrodynamic size of the nanocomposites after different calcinations (Fig. S13 and S14, ESI†). Various shades of light-gray to black crystal structures gradually appeared in the shell of the nanocomposites as the calcination temperature and the time increased, indicating the pore size variation. The hydrodynamic size of the nanocomposites after different calcinations between 400 °C and 600 °C was mainly in the range of 100–200 nm. But, the hydrodynamic size of the nanocomposites after calcination at 800 °C was mainly 1200 nm. The present

strategy of preparing PLMC with a tunable pore size and large mesopores will benefit the delivery of various types of drugs.

The PLMC obtained after 1 h of calcination at 500 °C was further characterized using elemental mapping, energy dispersive X-ray spectroscopy (EDS), and persistent luminescence measurements. Compared with PLNP@UiO-66, the as-prepared PLMC showed similar element distribution and a core–shell structure (Fig. 2a–h cf. Fig. S15, ESI†), but different molar ratios of C : O : Zn : Ga : Zr (0.9 : 3.2 : 1 : 1.8 : 2.7 cf. 3.9 : 3.5 : 1 : 1.8 : 2.1 for PLNP@UiO-66) (Fig. S16 and S17, Table S1, ESI†) due to the pyrolysis of the UiO-66 shell at 500 °C. The PLMC exhibited a little decreased persistent luminescence compared with the PLNP after UV light and LED excitation (Fig. S1 and S3, ESI†). However, the persistent luminescence signal can also be detected at 96 h after 10 min of UV excitation and at 48 h after 2 min of LED illumination on an IVIS Lumina III imaging system (Fig. S2 and S4, ESI†). The good persistent luminescence properties of PLMC indicate its potential in bioimaging applications. Therefore, PLMC obtained after calcination at 500 °C for 1 h was used for further bioimaging and drug delivery experiments.

Macrophage membrane camouflage and characterization of MPLMC

To realize targeted drug delivery and effective bioimaging-guided therapy, the J774A.1 macrophage membrane was coated on PLMC to obtain MPLMC (Fig. S18, ESI†) because the macrophage membrane coating can avoid the clearance of nanoparticles by the mononuclear phagocyte system and can overcome the vascular barrier.[43] The hydrodynamic size of the nanoparticles increased from 37.8 nm (PLNP) to 142.0 nm (MPLMC) (Fig. S19, ESI†). The zeta-potential changed from 23.3 mV (PLNP), 12.9 mV (PLNP@UiO-66), 12.2 mV (PLMC) to finally −28.4 mV (MPLMC) (Fig. S20, ESI†). Different nanoparticles and the functionalization of the macrophage membrane were further characterized through Fourier transform infrared (FT-IR) spectroscopy (Fig. S21, ESI†). The MPLMC not only showed vibration bands of Zn–O bending at 580 cm^{-1} and Ga–O bending at 460 cm^{-1} originating from the PLNP, but also gave absorption bands of the N–H stretching vibration at 3430 and 3280 cm^{-1}, the asymmetric and symmetric –CH_2– stretching vibrations at 2920 and 2850 cm^{-1}, the stretching vibration of –CO–NH– at 1650 cm^{-1}, and the stretching vibration

of C–N at 1004 cm^{-1} from the cell membranes, confirming the successful preparation of macrophage membrane-camouflaged PLMC. The dispersion stability of MPLMC and PLMC under the biological-mimicking conditions was investigated (Fig. S22, ESI†). The PLMC dispersion was very stable in both the PBS and DMEM cell culture media for 48 h, while the MPLMC showed a little increase in the hydrodynamic size distribution after dispersing in PBS at 48 h and a slight increase in the DMEM cell culture medium with time varying from 2 h to 48 h.

Drug loading and *in vitro* release properties of MPLMC

The drug loading and *in vitro* release properties of MPLMC were evaluated and compared with those of MPLNP@UiO-66. Doxycycline hydrochloride (Doxy), acetylsalicylic acid (ASA) and PTX were chosen as the model drugs to represent the hydrophilic, amphiphilic and hydrophobic molecules, respectively (Fig. 4a). The phosphorescence emission spectra (Fig. S23, ESI†) and the afterglow images (Fig. S24, ESI†) of the three model drug-loaded PLMC dispersions were compared to show whether the persistent luminescence performance of MPLMC was affected by the loaded drugs. MPLMC-ASA and MPLMC-PTX
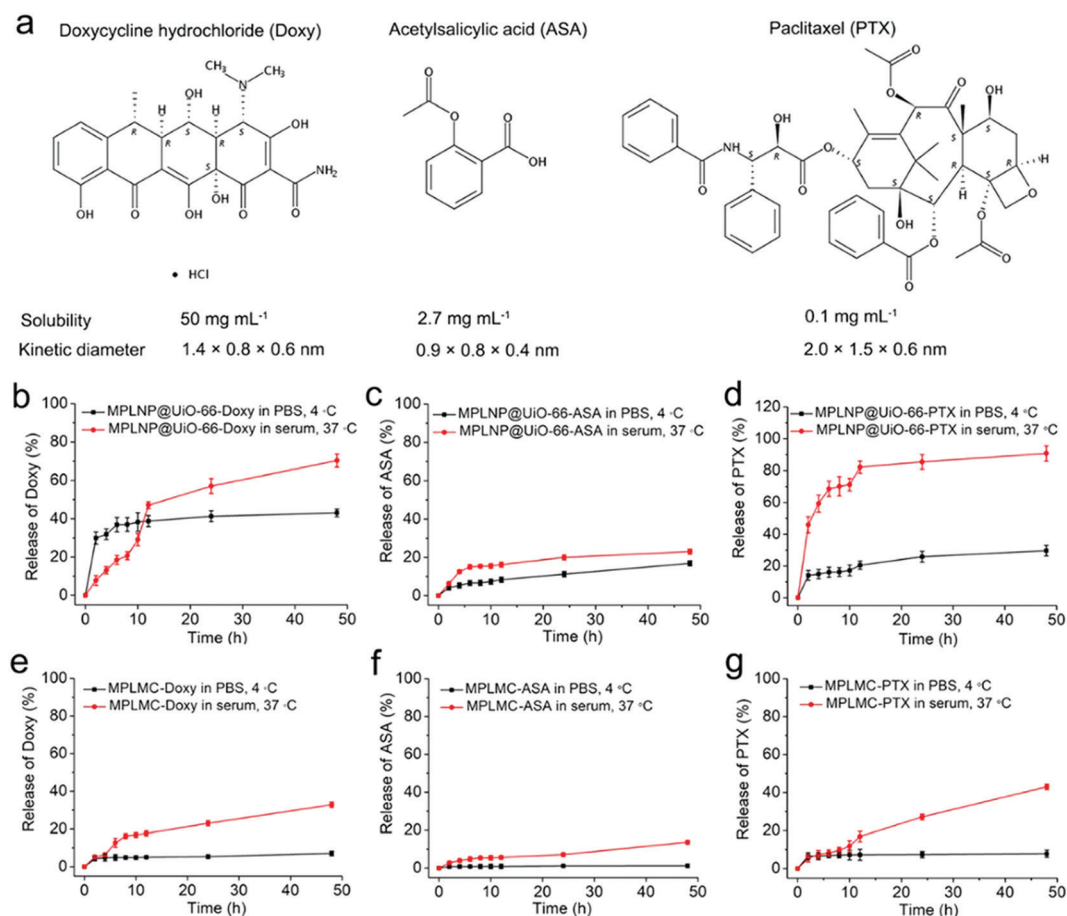

Fig. 4 Drug loading and release properties of MPLNP@UiO-66 and MPLMC: (a) chemical structural formula; water solubility; and the kinetic diameter of doxycycline hydrochloride (Doxy), acetylsalicylic acid (ASA), and paclitaxel (PTX). (b–g) *In vitro* drug release properties of Doxy-, ASA-, and PTX-loaded MPLNP@UiO-66 and MPLMC in PBS (10 mmol L^{-1}, pH 7.4) at 4 °C and under the simulated physiological conditions (human serum, 37 °C, shaken at 100 rpm).

showed good persistent luminescence similar to that of MPLMC, while MPLMC-Doxy showed decreased luminescence due to the broad absorption between 200 and 400 nm (Fig. S25, ESI†). MPLMC showed a larger drug loading capacity than MPLNP@UiO-66 (MPLNP@UiO-66-Doxy: 7.0 wt%; MPLMC-Doxy: 11.4 wt%; MPLNP@UiO-66-ASA: 14.3 wt%; MPLMC-ASA: 54.3 wt%; MPLNP@UiO-66-PTX: 1.1 wt%; MPLMC-PTX: 4.0 wt%). The results indicate that the PLMC can entrap more drugs especially the smallest ASA molecules due to the sufficiently large mesoporous pores. MPLMC showed stable and very low release of Doxy (7.1%), ASA (1.2%) and PTX (7.8%) (Fig. 4e–g), while MPLNP@UiO-66 exhibited high release efficiency of Doxy (43.1%), ASA (16.9%) and PTX (29.7%) after 48 h in PBS (10 mmol L^{-1}, pH 7.4) at 4 °C (Fig. 4b–d). Furthermore, Doxy-, ASA-, PTX-loaded MPLMC exhibited zero-order kinetics (Fig. 4e–g), whereas Doxy- and PTX-loaded MPLNP@UiO-66 showed first-order kinetic release in human serum media (Fig. 4b and d). Both ASA-loaded MPLNP@UiO-66 and MPLMC showed similar release behavior in human serum at 37 °C (under the simulated physiological conditions) (Fig. 4c and f). The observed different drug release behaviors were attributed to the different accessibilities of the UiO-66 and PLMC cavities for the drugs. The "burst release" manner in the first two hours for MPLNP-UiO-66-Doxy (Fig. 4b) and MPLNP-UiO-66-PTX (Fig. 4d) resulted from the Doxy and PTX mainly adsorbed on the surface of PLNP@UiO-66 with a relatively small pore window (*ca.* 1.1 nm). The different drug release behaviors were also influenced by the macrophage membrane coating on the external surface of PLNP@UiO-66 and PLMC.

The membrane coating provides a permeable lipid bilayer on the nanocomposite. The surface erosion, diffusion and swelling will gradually occur when the membrane-coated nanocomposites are dispersed in the serum medium or stimulated by the local environment, resulting in sustained and controlled release of the encapsulated drugs.[44] The drug release concentration of MPLMC sustained and linearly increased with time, which could facilitate controllable release in tumor therapy. These results indicate the great potential of MPLMC as a variable drug delivery carrier for the treatment of diseases. MPLMC-PTX was used in the following biological experiments.

In vitro cell imaging and cytotoxicity of MPLMC

To further verify the successful coating of the macrophage membrane on the PLMC and its stability, DiO-labeled MPLMC was incubated with SCC-7 cells (DiO is a green fluorescent probe for the cell membrane) and PLMC was used as the control (Fig. 5a). After incubation with MPLMC, both green fluorescence (DiO) and red luminescence (PLMC) were observed in the cytoplasm of the SCC-7 cells and matched well with each other. Meanwhile, no green fluorescence was found in the SCC-7 cells incubated with the uncoated PLMC. The results indicate the successful membrane coating on PLMC and the high stability of MPLMC in cellular uptake of the SCC-7 cells. To evaluate the cloaking ability of the macrophage membrane for the nanoparticles, the J774A.1 macrophages were individually incubated with PLMC, MPLMC and PLMC-PEG.

PLMC-PEG showed a similar negative surface charge (Fig. S19, ESI†) and particle dispersion (Fig. S20, ESI†) to those of MPLMC due to the biocompatible PEG-COOH modification. Cell imaging and flow cytometry analysis revealed that MPLMC showed much weaker luminescence of the PLNP than that of PLMC and PLMC-PEG in the J774A.1 macrophages (Fig. S26 and S27, ESI†). The result shows that the macrophage membrane coating significantly decreased the uptake of MPLMC.

The ability of MPLMC to cross an artificial endothelial layer *in vitro* was studied using transwell assay (Fig. 5b and c). MPLMC and PLMC were added in the confluent HUVEC layer for 8 h, in the absence and presence of TNF-α pretreatment, respectively. The SCC-7 cells in the lower chamber show strong red luminescence after MPLMC was added to the TNF-α treated HUVEC layer in the upper chamber (Fig. 5c). In contrast, no significant luminescence was observed in the other control groups (addition of PLMC to the HUVEC layer with TNF-α treatment, addition of MPLMC to the HUVEC layer without TNF-α treatment, and addition of PLMC to the HUVEC layer without TNF-α treatment). These results suggest that under simulative inflammation conditions macrophage membrane coating can facilitate the transport of the nanoparticles through an endothelial monolayer and increase the permeability of the vascular endothelial barrier. To evaluate the cytotoxicity of MPLMC, the cell counting kit-8 (CCK-8) method was used to examine the viability of the SCC-7 and HUVEC cells after incubation with different concentrations of MPLMC for 24 h. The cell viabilities were still over 97% even after being treated with a high concentration (500 μg mL^{-1}) of MPLMC (Fig. 5d). The *in vitro* therapeutic potential of MPLMC-PTX was also assessed using the same method. The cell viabilities of the SCC-7 and HUVEC treated cells with MPLMC-PTX decreased to 49.9% and 50.1%, respectively, and even with a low PTX concentration (3.9 μg mL^{-1}, 100 μg mL^{-1} as PLMC) (Fig. 5e). Both propidium iodide (PI) staining (Fig. 5f) and flow cytometry analysis (Fig. 5g and Fig. S28, ESI†) revealed that the SCC-7 cells treated with MPLMC-PTX (500 μg mL^{-1} as PLMC) showed the most significant luminescence of PI, proving the high cytotoxicity of MPLMC-PTX.

In vivo imaging of MPLMC in the SCC-7 tumor model

The ability of MPLMC to evade the mononuclear phagocyte system and accumulate in tumors was studied *in vivo* based on the persistent luminescence of PLNP without *in situ* excitation on an IVIS Lumina imaging system. Luminescence signals appeared in the liver and lungs (two of the reticuloendothelial system organs) of mice in both the experiment group (injection with MPLMC) and control group (injection with PLMC). The intravenously administered-PLMC mice group showed strong luminescence in the liver at 1 h after injection, while the MPLMC-administered mice group showed delayed accumulation in the liver in the initial 2 h after injection, indicating the biomimetic camouflage ability of the J774A.1 membrane on MPLMC (Fig. 6a). However, tumor-targeting accumulation of MPLMC in SCC-7 tumor-bearing mice was obviously enhanced compared with that in the control group. The luminescence
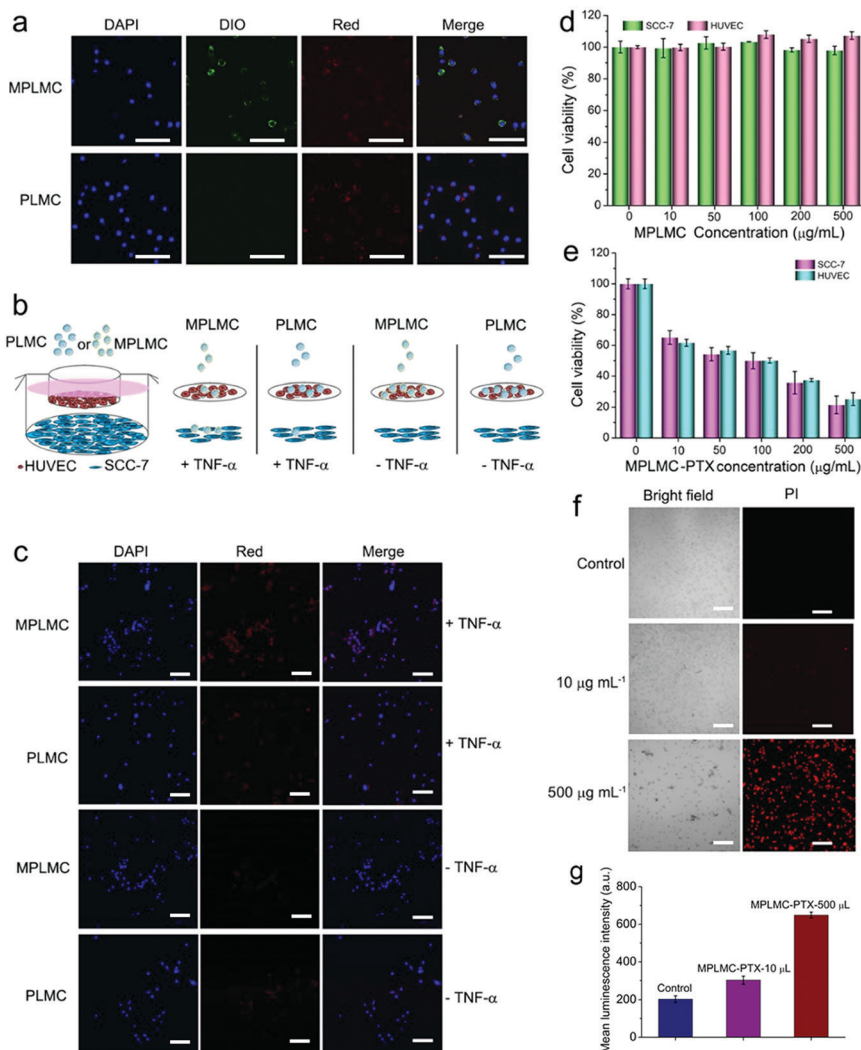
Fig. 5 Cell imaging and cytotoxicity: (a) confocal microscopy images of SCC-7 cells incubated with MPLMC or PLMC, respectively. The green color came from the DiO dye for macrophage membrane staining. The red color resulted from the PLMC, showing their intracellular location. The blue color represented cellular nuclei staining with DAPI. Scale bar, 100 μm. (b) Schematic of a transwell chamber for assaying nanoparticle transport across an endothelial cell monolayer. (c) Representative confocal microscopy images of SCC-7 (cancer) cells in the lower chamber under the surface of TNF-α treated or untreated HUVEC (endothelial) after incubation with MPLMC or PLMC. Scale bar, 100 μm. (d) Cell viability studies of HUVEC and SCC-7 incubated with different concentrations of MPLMC. (e) *In vitro* cytotoxicity of HUVEC and SCC-7 treated with different concentrations (calculated as MPLMC) of MPLMC-PTX. (f) Confocal microscopy images of SCC-7 cells treated with different concentrations of MPLMC-PTX. PI stained the dead cells. Scale bar, 100 μm. (g) Mean luminescence intensity of the J774A.1 macrophages treated with various concentrations of MPLMC-PTX measured and analyzed by flow cytometry.

signal appeared on the tumors at 1 h, increased significantly at 2 h and remained till 6 h after MPLMC administration. The luminescence intensity decreased with time but could still be observed at 48 h post-injection. However, no significant luminescence was observed in the tumors of mice from the control group, indicating that the MPLMC adhered to the tumor endothelium with the aid of the J774A.1 macrophage membrane cloaking ability.

The *ex vivo* afterglow images of the major organs from the two mice groups were obtained at 24 and 48 h post-injection (Fig. 6b–e). The analyzed results show that the luminescence intensity of MPLMC accumulation in the liver at 24 h was higher than that of the PLMC injection group by 1.4 times, and it significantly decreased by 0.6 times at 48 h. However, the

luminescence intensity of PLMC accumulation in the spleen and lungs at 24 h was 2.1- and 1.5-fold greater than that of the experimental group, still 1.0- and 1.9-fold compared with the experimental group at 48 h. The results indicate the low adherence of MPLMC to the reticuloendothelial system organs after macrophage membrane camouflage. Meanwhile, the autofluorescence-free bioimaging of PLMC provides important guidance for further drug therapy.

In vivo therapeutic ability of MPLMC-PTX and the toxic study of MPLMC

The *in vivo* therapeutic ability of MPLMC-PTX to inhibit tumor growth was evaluated. The tumor *ex vivo* photographs and
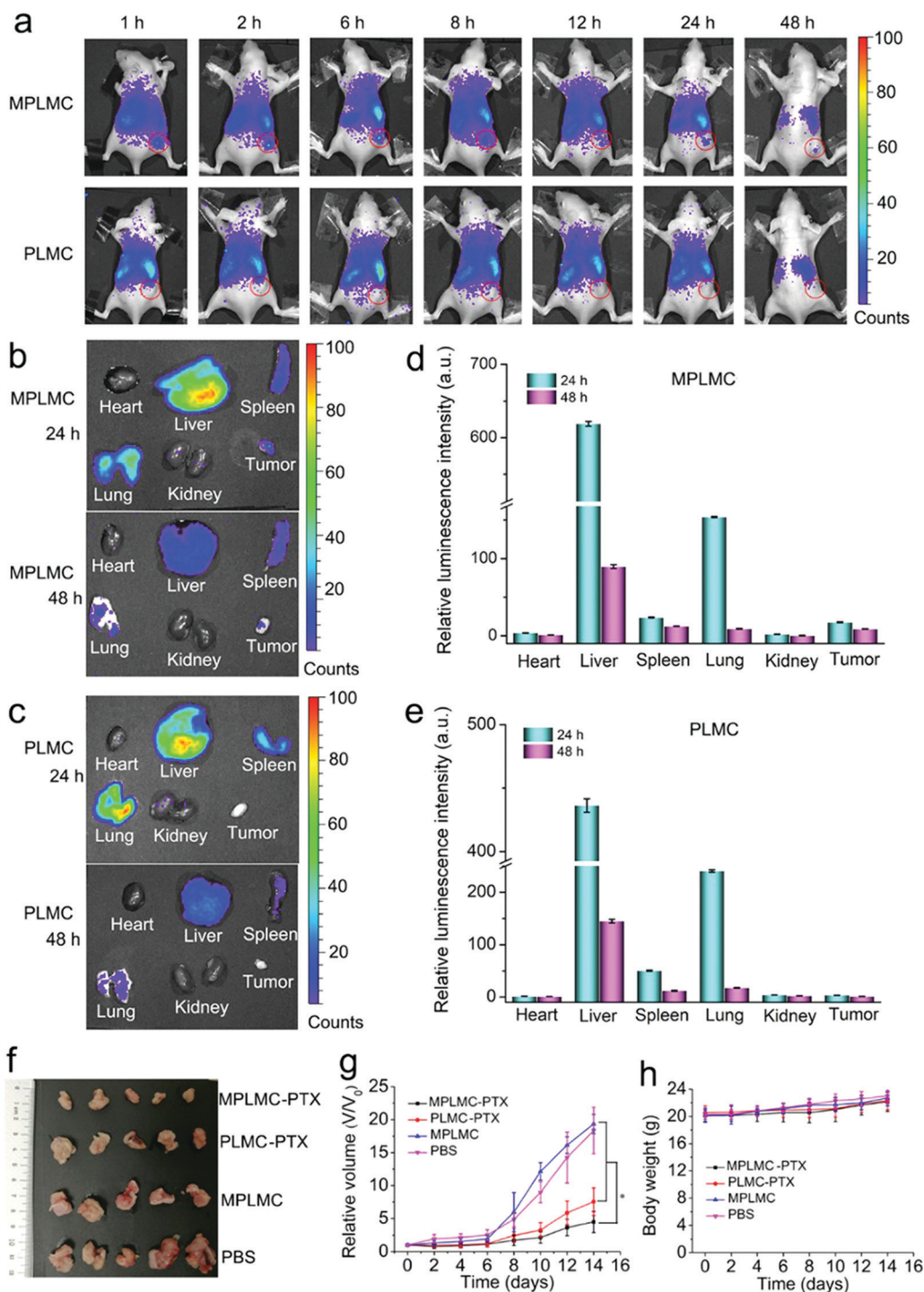
Fig. 6 *In vivo* afterglow imaging (2 min of LED illumination before each acquisition) and chemotherapy of SCC-7 tumor-bearing mice: (a) afterglow images of MPLMC and PLMC for time-dependent distribution in mice after intravenous injection. (b) *Ex vivo* afterglow images of the major organs and tumors dissected from mice at 24 and 48 h after intravenous injection with MPLMC. (c) *Ex vivo* afterglow images of the major organs and tumors dissected from mice at 24 and 48 h after intravenous injection with PLMC. (d) Relative luminescence intensity of the major organs and tumors dissected from mice at 24 and 48 h pre-injected with MPLMC. (e) Relative luminescence intensity of the major organs and tumors dissected from mice at 24 and 48 h pre-injected with PLMC. The luminescence intensity of the heart at 48 h was set as the control. Data were calculated as mean $\pm$ standard deviation (n = 3). (f) SCC-7 tumor photographs dissected from mice of different treatment groups after 14 days. (g) SCC-7 tumor growth curves of different treatment groups. $P < 0.05$. (h) Body weight of the variation of mice from different treatment groups.

growth curves with time (Fig. 6f and g) show that tumor growth was significantly inhibited in the MPLMC-PTX and PLMC-PTX

administered groups, while enhanced inhibition was observed in MPLMC-PTX compared to PLMC-PTX. The results suggest

the drug efficacy of PTX and the superior tumor accumulation of MPLMC. Hematoxylin and eosin (H&E) staining confirms that MPLMC-PTX injection induced a significant necrotic response in the tumor tissues (Fig. S29, ESI†). No remarkable difference was seen in the body weight change with time (Fig. 6h), and no damage sign was found upon H&E staining of the major organs in healthy mice after intravenous injection with MPLMC, PLMC and PBS, respectively (Fig. S30, ESI†). These results suggest that MPLMC is a promising kind of drug delivery carrier for *in vivo* applications.

Conclusions

In summary, we have reported a facile and bio-friendly synthesis of a macrophage membrane camouflaged core–shell NIR-emitting PLNP@MOF-derived MC nanocomposite (PLMC) with a controllable mesopore size for drug encapsulation and luminescence imaging-guided chemotherapy. The developed PLMC shows a nanoscale diameter smaller than 100 nm, a controllable shell layer, a tunable large mesopore size, and renewable NIR persistent luminescence, indicating that it is a promising candidate as a luminescence trackable drug delivery carrier. Moreover, biomimetic macrophage membrane coating on the nanocomposite (MPLMC) shows a long circulation lifetime and enhanced tumor-targeting ability *in vivo*. MPLMC-PTX provides autofluorescence-free imaging and effective tumor inhibition. The developed strategy will open up a new direction to design integrated nanoconjugates as powerful tools featuring persistent luminescence and high drug loading capacity for individualized treatment applications.

Conflicts of interest

The authors declare no competing financial interest.

Acknowledgements

References

1 E. Blanco, H. Shen and M. Ferrari, *Nat. Biotechnol.*, 2015, **33**, 941–951.

2 P. Dong, K. P. Rakesh, H. M. Manukumar, Y. H. E. Mohammed, C. S. Karthik, S. Sumathi, P. Mallu and H. L. Qin, *Bioorg. Chem.*, 2019, **85**, 325–336.

3 J. E. Lee, N. Lee, H. Kim, J. Kim, S. H. Choi, J. H. Kim, T. Kim, I. C. Song, S. P. Park, W. K. Moon and T. Hyeon, *J. Am. Chem. Soc.*, 2010, **132**, 552–557.

4 C. T. Matea, T. Mocan, F. Tabaran, T. Pop, O. Mosteanu, C. Puia, C. Iancu and L. Mocan, *Int. J. Nanomed.*, 2017, **12**, 5421–5431.

5 J. Liu, W. Bu, L. Pan and J. Shi, *Angew. Chem. Int. Ed.*, 2013, **52**, 4375–4379.

6 T. Maldiney, A. Bessiere, J. Seguin, E. Teston, S. K. Sharma, B. Viana, A. J. Bos, P. Dorenbos, M. Bessodes, D. Gourier, D. Scherman and C. Richard, *Nat. Mater.*, 2014, **13**, 418–426.

7 S. K. Sun, H. F. Wang and X. P. Yan, *Acc. Chem. Res.*, 2018, **51**, 1131–1143.

8 Y. Li, M. Gecevicius and J. Qiu, *Chem. Soc. Rev.*, 2016, **45**, 2090–2136.

9 W. Jiang, L. Huang, F. Mo, Y. Zhong, L. Xu and F. Fu, *J. Mater. Chem. B*, 2019, **7**, 3019–3026.

10 F.-X. Su, X. Zhao, C. Dai, Y.-J. Li, C.-X. Yang and X.-P. Yan, *Chem. Commun.*, 2019, **55**, 5283–5286.

11 Y. M. Yang, Z. Y. Li, J. Y. Zhang, Y. Lu, S. Q. Guo, Q. Zhao, X. Wang, Z. J. Yong, H. Li, J. P. Ma, Y. Kuroiwa, C. Moriyoshi, L. L. Hu, L. Y. Zhang, L. R. Zheng and H. T. Sun, *Light: Sci. Appl.*, 2018, **7**, 88.

12 Z. Pan, Y. Y. Lu and F. Liu, *Nat. Mater.*, 2011, **11**, 58–63.

13 A. Abdukayum, J.-T. Chen, Q. Zhao and X.-P. Yan, *J. Am. Chem. Soc.*, 2013, **135**, 14125–14133.

14 A. Bessière, S. K. Sharma, N. Basavaraju, K. R. Priolkar, L. Binet, B. Viana, A. J. J. Bos, T. Maldiney, C. Richard, D. Scherman and D. Gourier, *Chem. Mater.*, 2014, **26**, 1365–1373.

15 Z. Li, Y. Zhang, X. Wu, L. Huang, D. Li, W. Fan and G. Han, *J. Am. Chem. Soc.*, 2015, **137**, 5304–5307.

16 J. Shi, M. Sun, X. Sun and H. Zhang, *J. Mater. Chem. B*, 2016, **4**, 7845–7851.

17 R. Zou, S. Gong, J. Shi, J. Jiao, K.-L. Wong, H. Zhang, J. Wang and Q. Su, *Chem. Mater.*, 2017, **29**, 3938–3946.

18 J. Wang, J. Li, J. Yu, H. Zhang and B. Zhang, *ACS Nano*, 2018, **12**, 4246–4258.

19 L. J. Chen, C. X. Yang and X. P. Yan, *Anal. Chem.*, 2017, **89**, 6936–6939.

20 Y. Fang, G. Zheng, J. Yang, H. Tang, Y. Zhang, B. Kong, Y. Lv, C. Xu, A. M. Asiri, J. Zi, F. Zhang and D. Zhao, *Angew. Chem. Int. Ed.*, 2014, **53**, 5366–5370.

21 T. Simon-Yarza, A. Mielcarek, P. Couvreur and C. Serre, *Adv. Mater.*, 2018, **30**, e1707365.

22 J. D. Rocca, D. Liu and W. Lin, *Acc. Chem. Res.*, 2011, **44**, 957–968.

23 Y. Lv, D. Ding, Y. Zhuang, Y. Feng, J. Shi, H. Zhang, T. L. Zhou, H. Chen and R. J. Xie, *ACS Appl. Mater. Interfaces*, 2018, **11**, 1907–1916.

24 H. Zhao, G. Shu, J. Zhu, Y. Fu, Z. Gu and D. Yang, *Biomaterials*, 2019, **217**, 119332.

25 T. Kundu, S. Mitra, P. Patra, A. Goswami, D. Diaz Diaz and R. Banerjee, *Chem. – Eur. J.*, 2014, **20**, 10514–10518.

26 P. Horcajada, T. Chalati, C. Serre, B. Gillet, C. Sebrie, T. Baati, J. F. Eubank, D. Heurtaux, P. Clayette, C. Kreuz, J. S. Chang, Y. K. Hwang, V. Marsaud, P. N. Bories, L. Cynober, S. Gil, G. Ferey, P. Couvreur and R. Gref, *Nat. Mater.*, 2010, **9**, 172–178.

27 M. X. Wu and Y. W. Yang, *Adv. Mater.*, 2017, **29**, 1606134.

28 T.-W. Kim, P.-W. Chung, I. I. Slowing, M. Tsunoda, E. S. Yeung and V. S.-Y. Lin, *Nano Lett.*, 2008, **8**, 3724–3727.

29 L. Zhou, Y. Jing, Y. Liu, Z. Liu, D. Gao, H. Chen, W. Song, T. Wang, X. Fang, W. Qin, Z. Yuan, S. Dai, Z. A. Qiao and C. Wu, *Theranostics*, 2018, **8**, 663–675.

30 J. Gu, S. Su, Y. Li, Q. He and J. Shi, *Chem. Commun.*, 2011, **47**, 2101–2103.

31 Y. Chen, P. Xu, M. Wu, Q. Meng, H. Chen, Z. Shu, J. Wang, L. Zhang, Y. Li and J. Shi, *Adv. Mater.*, 2014, **26**, 4294–4301.

32 J. Liu, N. P. Wickramaratne, S. Z. Qiao and M. Jaroniec, *Nat. Mater.*, 2015, **14**, 763–774.

33 Y. Fang, D. Gu, Y. Zou, Z. Wu, F. Li, R. Che, Y. Deng, B. Tu and D. Zhao, *Angew. Chem. Int. Ed.*, 2010, **49**, 7987–7991.

34 J. Zhu, L. Liao, X. Bian, J. Kong, P. Yang and B. Liu, *Small*, 2012, **8**, 2715–2720.

35 B. Liu, H. Shioyama, T. Akita and Q. Xu, *J. Am. Chem. Soc.*, 2008, **130**, 5390–5391.

36 C. C. Hou, L. Zou and Q. Xu, *Adv. Mater.*, 2019, 1904689.

37 Q. Yang, C. C. Yang, C. H. Lin and H. L. Jiang, *Angew. Chem. Int. Ed.*, 2019, **58**, 3511–3515.

38 Z. Zhou, W. Zheng, J. Kong, Y. Liu, P. Huang, S. Zhou, Z. Chen, J. Shi and X. Chen, *Nanoscale*, 2017, **9**, 6846–6853.

39 L.-J. Chen, X. Zhao and X.-P. Yan, *ACS Appl. Mater. Interfaces*, 2019, **11**, 19894–19901.

40 M. Allix, S. Chenu, E. Véron, T. Poumeyrol, E. A. Kouadri-Boudjelthia, S. Alahraché, F. Porcher, D. Massiot and F. Fayon, *Chem. Mater.*, 2013, **25**, 1600–1606.

41 Y. Liu, Y. Yang, Y. Sun, J. Song, N. G. Rudawski, X. Chen and W. Tan, *J. Am. Chem. Soc.*, 2019, **141**, 7407–7413.

42 F. Heshmatpour and R. B. Aghakhanpour, *Adv. Powder Technol.*, 2012, **23**, 80–87.

43 A. Parodi, N. Quattrocchi, A. L. van de Ven, C. Chiappini, M. Evangelopoulos, J. O. Martinez, B. S. Brown, S. Z. Khaled, I. K. Yazdi, M. V. Enzo, L. Isenhart, M. Ferrari and E. Tasciotti, *Nat. Nanotechnol.*, 2013, **8**, 61–68.

44 B. T. Luk and L. Zhang, *J. Controlled Release*, 2015, **220**, 600–607.